

Engineering Nitrogen-Doped Carbon Quantum Dots: Tailoring Optical and Chemical Properties through Selection of Nitrogen Precursors

Kiem G. Nguyen, Matej Huš, Ioan-Alexandru Baragau, James Bowen, Tobias Heil, Adela Nicolaev, Laura Elena Abramiuc, Andrei Sapelkin, Muhammad Tariq Sajjad, and Suela Kellici*

The process of N-doping is frequently employed to enhance the properties of carbon quantum dots. However, the precise requirements for nitrogen precursors in producing high-quality N-doped carbon quantum dots (NCQDs) remain undefined. This research systematically examines the influence of various nitrogen dopants on the morphology, optical features, and band structure of NCQDs. The dots are synthesized using an efficient, eco-friendly, and rapid continuous hydrothermal flow technique. This method offers unparalleled control over synthesis and doping, while also eliminating convention-related issues. Citric acid is used as the carbon source, and urea, trizma base, beta-alanine, L-arginine, and EDTA are used as nitrogen sources. Notably, urea and trizma produced NCQDs with excitation-independent fluorescence, high quantum yields (up to 40%), and uniform dots with narrow particle size distributions. Density functional theory (DFT) and time-dependent DFT modelling established that defects and substituents within the graphitic structure have a more significant impact on the NCQDs' electronic structure than nitrogen-containing functional groups. Importantly, for the first time, this work demonstrates that the conventional approach of modelling single-layer structures is insufficient, but two layers suffice for replicating experimental data. This study, therefore, provides essential guidance on the selection of nitrogen precursors for NCQD customization for diverse applications.


1. Introduction

Carbon quantum dots (CQDs) have emerged as a promising class of nanomaterials with applications in optoelectronics, biomedicine, and sensing. Their unique optical, electronic, and chemical properties, such as high photoluminescence, low toxicity, and easy functionalization, make them attractive for targeted applications.^[1] However, the photoluminescence quantum yield (QY) of CQDs remains a challenge that limits their practical applications. To address this challenge, doping carbon quantum dots with heteroatoms, particularly nitrogen, has shown to efficiently enhance the optical properties of CQDs. Nitrogen dopants offer suitable atomic size for doping into CQD structures, strong electronegativity allowing beneficial interaction with carbon, and an accessible lone pair of electrons that enables effective tuning of the CQDs' electronic properties.^[2] While nitrogen dopants have become essential to produce high-quality nitrogen doped carbon quantum dots (NCQDs),^[3]

K. G. Nguyen, I.-A. Baragau, M. T. Sajjad, S. Kellici
School of Engineering
London South Bank University
103 Borough Road, London SE1 0AA, UK
E-mail: kellcicis@lsbu.ac.uk

M. Huš
Department of Catalysis and Chemical Reaction Engineering
National Institute of Chemistry
Ljubljana SI-1001, Slovenia

M. Huš
Association for Technical Culture of Slovenia (ZOTKS)
Zaloška 65, Ljubljana 1000, Slovenia

 The ORCID identification number(s) for the author(s) of this article can be found under <https://doi.org/10.1002/smll.202310587>

© 2024 The Authors. Small published by Wiley-VCH GmbH. This is an open access article under the terms of the [Creative Commons Attribution License](https://creativecommons.org/licenses/by/4.0/), which permits use, distribution and reproduction in any medium, provided the original work is properly cited.

DOI: 10.1002/smll.202310587

M. Huš
Institute for the Protection of Cultural Heritage of Slovenia (ZVKDS)
Poljanska 40, Ljubljana 1000, Slovenia

I.-A. Baragau, A. Nicolaev, L. E. Abramiuc
National Institute of Materials Physics
Atomistilor 405A, Magurele, Ilfov 077125, Romania

J. Bowen
School of Engineering and Innovation
Open University
Walton Hall, Milton Keynes MK7 6AA, UK

T. Heil
Department of Colloid Chemistry
Max Planck Institute of Colloids and Interfaces
14476 Potsdam, Germany

A. Sapelkin
School of Physical and Chemical Sciences
Queen Mary University of London
Mile End Road, London E1 4NS, UK

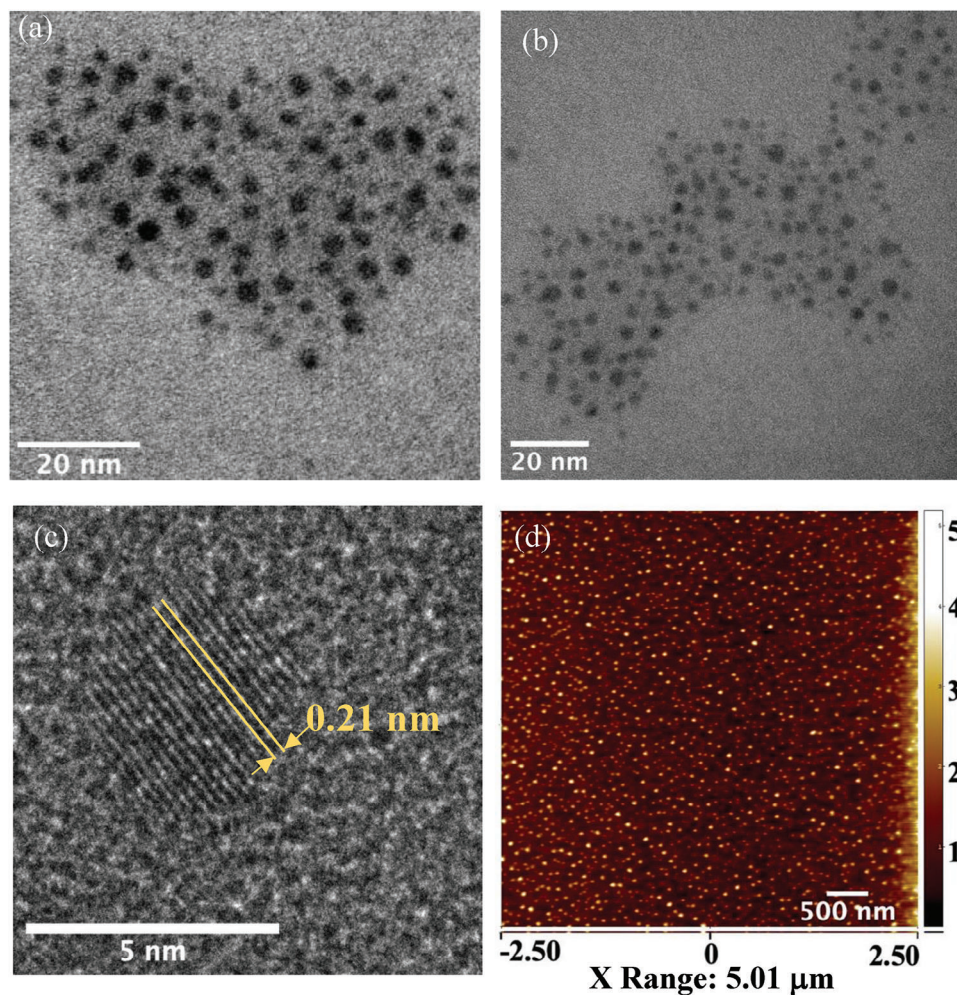


Figure 1. HR-TEM images of NCQDs-Urea and trizma base at different magnifications: a) NCQDs-Trizma, b) NCQDs-Urea, c) graphitic core lattices with d-spacing of 0.21 ± 0.01 nm, and d) AFM images of NCQDs-Urea.

there is a lack of comparison between different nitrogen sources and unclear mechanism of the doping processes due to the variation of synthetic methods and limitation to certain types of nitrogen precursors.^[4,5] The type of nitrogen precursor influences the nitrogen content and bonding configuration in NCQDs, which in turn impacts the particle size, optical properties, and electronic structure.^[6,7] Therefore, further studies are needed.

In addition to selecting appropriate precursors, the synthetic process itself is vital for achieving an efficient production method for NCQDs. Conventional CQD fabrication processes are often time and energy consuming, and they provide poor control over the final particle properties. To overcome these limitations, the Continuous Hydrothermal Flow Synthesis method (CHFS) has gained prominence.^[8,9,10] CHFS offers several advantages over the traditional hydrothermal synthesis, including unparalleled control over synthesis and doping, shorter reaction times, tunability, higher yields and enhanced optical properties (e.g., controllable excitation independent emission and increased quantum yield).^[11,12] It provides a toolbox for the rapid development of carbon nanodots engineered for targeted applications.

In this study, we aim to systematically investigate how different nitrogen precursors impact the properties of NCDQs synthesized via CHFS. The nitrogen precursors utilized include urea, β -alanine, L-arginine, ethylenediaminetetraacetic acid dipotassium salt dihydrate (EDTA), and trizma base. Urea is a common, cost-effective nitrogen precursor that is readily available.^[13] β -alanine and L-arginine, inexpensive amino acids, are expected to introduce beneficial nitrogen functionalities for doping CQDs. The amino groups act as reactive sites for controlled nucleation and growth of dots. Additionally, the carboxylic acid and guanidine side chains enable surface passivation for enhanced hydrophilicity, colloidal stability, and photoluminescence. The biocompatibility of β -alanine and L-arginine also imparts low cytotoxicity for the synthesized NCQDs.^[14,15] EDTA, a chelating agent, has the potential to form stable complexes with CQDs,^[16] while trizma base with its hydroxyl/amine reactivity, excellent solubility, and ability to dope and passivate, is an excellent nitrogen precursor for engineering high quality fluorescent NCQDs.^[17]

Through this study, we aim to enhance our understanding of the NCQDs synthesis process by shedding light on the early-stage processes of NCQDs formation, which are crucial for

Table 1. The mean particle size of the prepared NCQDs.

Sample	Particle size [nm]
NCQDs-Urea	3.5 ± 0.8
NCQDs-Alanine	2.4 ± 1.3
NCQDs-Arginine	2.9 ± 1.2
NCQDs-EDTA	4.0 ± 1.7
NCQDs-Trizma	3.4 ± 0.7

optimizing their properties. Moreover, to complement our experimental findings and characterizations, we employ state-of-the-art modelling techniques to study the structural, electronic, and optical characteristics of NCQDs. The combination of experimental data and advanced modelling allows for a comprehensive investigation into the formation, growth, and properties of NCQDs, contributing to the advancement of this versatile class of nanomaterials. It provides a roadmap for the rapid development of CQDs tailored for various applications.

2. Results and Discussion

2.1. The Morphology and Chemical Properties of NCQDs

High-resolution TEM (HR-TEM) and atomic force microscopy (AFM) imaging revealed significant variations in the size and distribution of the synthesized NCQDs depending on the nitrogen source used. The HR-TEM images in **Figure 1** illustrate the round shape and uniformity of NCQDs-Urea sample as well as lattice spacing of 0.21 ± 0.01 nm corresponding to the graphitic core.^[9] This finding aligns with our previous reports, further confirming the effectiveness and reliability of the CHFS method for

NCQDs synthesis.^[11] The similar observations for trizma sample suggest that both precursors serve as effective nitrogen sources. Conversely, NCQDs prepared with alanine, arginine and EDTA as dopants revealed amorphous SAED patterns (Figure S1, Supporting Information). Additional information relating to the morphology, topography and particle size analysis was provided by AFM images (Figure 1d and Figure S2, Supporting Information).

The nanoparticle size analysis derived from the microscopy imaging techniques (**Table 1** and **Figure 2**) shows the influence of nitrogen dopants on NCQDs properties. **Figure 2b** displays the particle size distribution of NCQDs-Alanine, which has the smallest mean particle size (2.4 ± 1.3 nm) and a broad distribution (1.0–8.0 nm). NCQDs-Arginine exhibited a slightly larger average particle size (2.9 ± 1.2 nm), with a range of 1.0–6.0 nm (**Figure 2c**). Both samples showed skewed distributions, with modes below 3.0 nm.

In contrast, NCQDs-EDTA (**Figure 2d**) displayed a multimodal histogram (4.0 ± 1.7 nm, range 1.0–7.0 nm), indicating varied populations. Image analysis of NCQDs-Urea and NCQDs-Trizma samples (**Figure 2a,b**) revealed symmetric histograms and a narrow size distribution, indicating a high degree of uniformity in particle sizes (ranging from 2.5 to 5.5 nm). The differences in the size and distribution of nanoparticles among NCQDs-Urea, NCQDs-Trizma, NCQDs-Arginine, and NCQDs-EDTA are expected to result in distinct optical properties for the NCQDs. Further investigation and analysis of these materials are crucial for understanding the influence of N-dopants on carbon quantum dots.

Figure 3a shows the FTIR spectra of NCQDs, providing evidence of characteristic nitrogen and oxygen functional groups, confirming the successful N-doping of carbon quantum dots. Across all spectra, a broad band ranging from 2600 to 3500 cm^{-1}

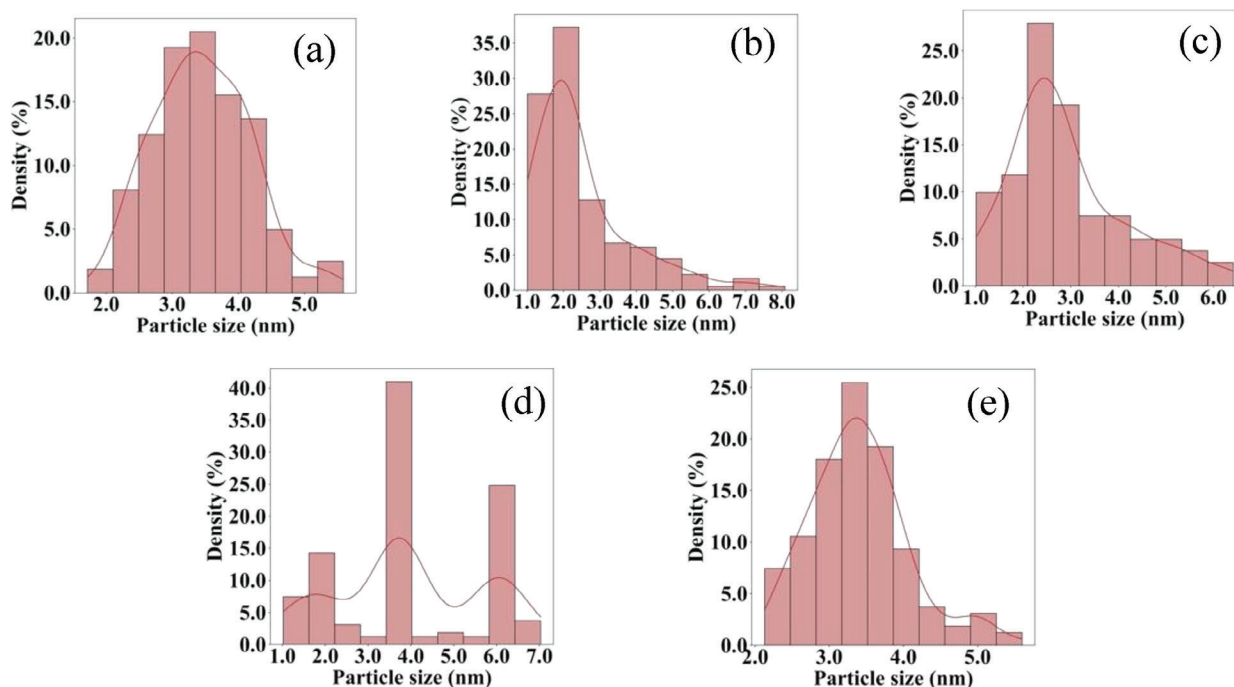


Figure 2. Particle size distribution histograms for: a) NCQDs-Urea, b) NCQDs-Alanine, c) NCQDs-Arginine, d) NCQDs-EDTA, and e) NCQDs-Trizma.

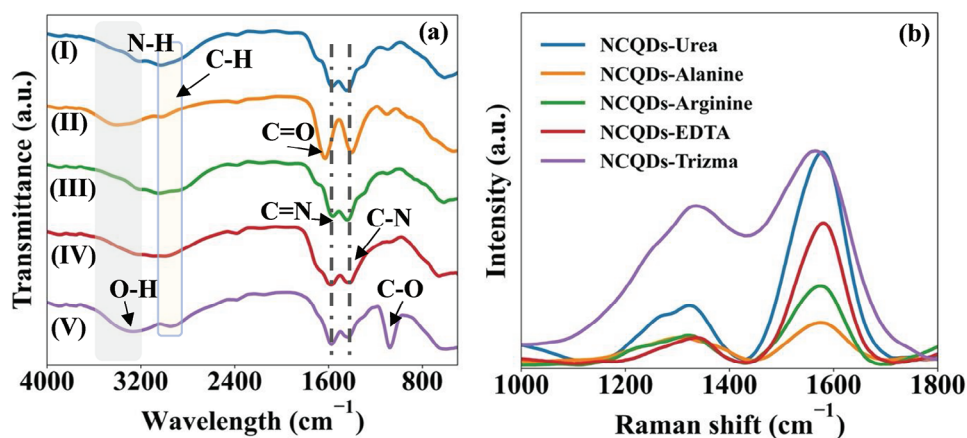


Figure 3. a) FT-IR spectra of: I) NCQDs-Urea, II) NCQDs-Alanine, III) NCQDs-Arginine, IV) NCQDs-EDTA, and V) NCQDs-Trizma; b) Raman spectra of the synthesized NCQDs.

is observed, corresponding to overlapping stretches encompassing various vibrations. These include the O–H bond (–COOH, R–OH) commonly found between 3250 and 3500 cm^{-1} ,^[18] as well as amine/protonated amine (N–H) vibrations. Additionally, a broad peak below 3000 cm^{-1} can be attributed to the C–H bond.^[19] The NCQDs-Alanine sample prominently exhibits the presence of the C–O bond ($\approx 1650 \text{ cm}^{-1}$). The NCQDs exhibited a band at 1575 cm^{-1} corresponding to the stretching vibration of C=N bond.^[20] In the fingerprint region, the peak at 1450 cm^{-1} confirms the presence of C–N bond. The spectrum of NCQDs-Trizma displays a peak at 1100 cm^{-1} associated with the vibration of the C–O bond, while this peak is less pronounced in the other NCQDs.^[21,22]

Moreover, in addition to FT-IR analysis discussed, the Raman spectra of NCQDs (Figure 3b) provide further insight into the structural properties of these samples. The spectra show characteristic D and G bands originating from the carbon core. The G band, located $\approx 1580 \text{ cm}^{-1}$ corresponds to the E_{2g} vibrational mode of sp^2 graphitic carbon domains, indicating crystalline graphitic structures within the NCQDs. The D band located at $\approx 1350 \text{ cm}^{-1}$ is associated with structural defects and discontinuities in the carbon framework. Interestingly, the NCQDs-Urea and NCQDs-Trizma samples exhibit relatively lower I_D/I_G ratios (Figure S3, Supporting Information) indicating a higher quality graphitic content in these samples. These findings are consistent with the results obtained from HR-TEM, which also confirmed the graphitic crystalline nature for these NCQDs.

Furthermore, XPS investigation was carried out to determine the chemical composition of the samples. The core level spectra were deconvoluted with use of Voigt functions (which incorporate Lorentzian and Gaussian widths along with a distinctive inelastic background for each component). A minimum number of components was selected to achieve an optimal fit for the spectra. The binding energy scale was calibrated based on the C1s standard value of 284.6 eV. The XPS spectra (Figure S4, Supporting Information) display three typical binding energies ascribed to C1s at 285 eV, O1s at 531 eV and N1s at 399 eV.

The high resolution N1s XPS spectra of the NCQDs (Figure 4) fitted with three Gaussian peaks revealed a predominant peak located at the region 398.6–399.5 eV, which is assigned

to pyrrolic N, another peak at 396.8–397.0 eV attributed to pyridinic N in an aromatic, and a third peak at 400.1–400.4 eV indicated the presence of hydrogenated pyridinic nitrogen.^[21] In the NCQDs-Alanine sample the presence of N-graphitic is noted at 401.10 eV. The deconvolution of the high-resolution C 1s spectra (Figures S4–S9, Supporting Information) indicated the presence of C=C sp^2 at 284.5 eV, C–O/C–N sp^3 at 286.5 eV, and C=N/C=O at 287.7 eV. This XPS data analysis aligns well with the mentioned FT-IR characterization.

While urea and trizma base contain lower carbon content compared to the other nitrogen precursors, XPS data (Figure 5a) revealed a high carbon content in the corresponding nitrogen-doped carbon quantum dots (NCQDs-Urea and NCQDs-Trizma). This confirms that urea and trizma enabled efficient carbonization of the citric acid precursor despite having less intrinsic carbon. Analysis of the relative ratios of carbon, nitrogen, and oxygen (C/N and C/O) shown in Table S2, Supporting Information, provides details into the composition and surface chemistry of the synthesized NCQDs. Urea, β -alanine and L-arginine, with higher N atom counts, led to N-CQDs with lower C/N ratios, and greater overall nitrogen incorporation into the carbon core. Meanwhile, the C/O ratio was highest for the NCQDs prepared using arginine, suggesting higher surface oxygen groups. This demonstrates the ability to control doping levels and surface chemistry by tuning the nitrogen precursor.

2.2. The Optical Properties of NCQDs

The effect of the nitrogen dopants on the optical properties of NCQDs was further investigated using UV–vis and fluorescence spectrophotometry. The UV–vis absorbance of the synthesized NCQDs was measured in a 10 mm quartz cuvette using deionized water as reference, and the corresponding spectra for different NCQDs are given in Figure 6. Notably, the NCQDs-Alanine, Arginine, EDTA and Trizma samples exhibit similar absorption spectra, featuring a broad absorption band from 275 to 375 nm, centered between 300 and 350 nm. This absorption band is attributed to the $n\text{-}\pi^*$ transitions of C=N bonding, and a shoulder at 290 nm is assigned to the transitions of $\pi\text{-}\pi^*$ of the aromatic

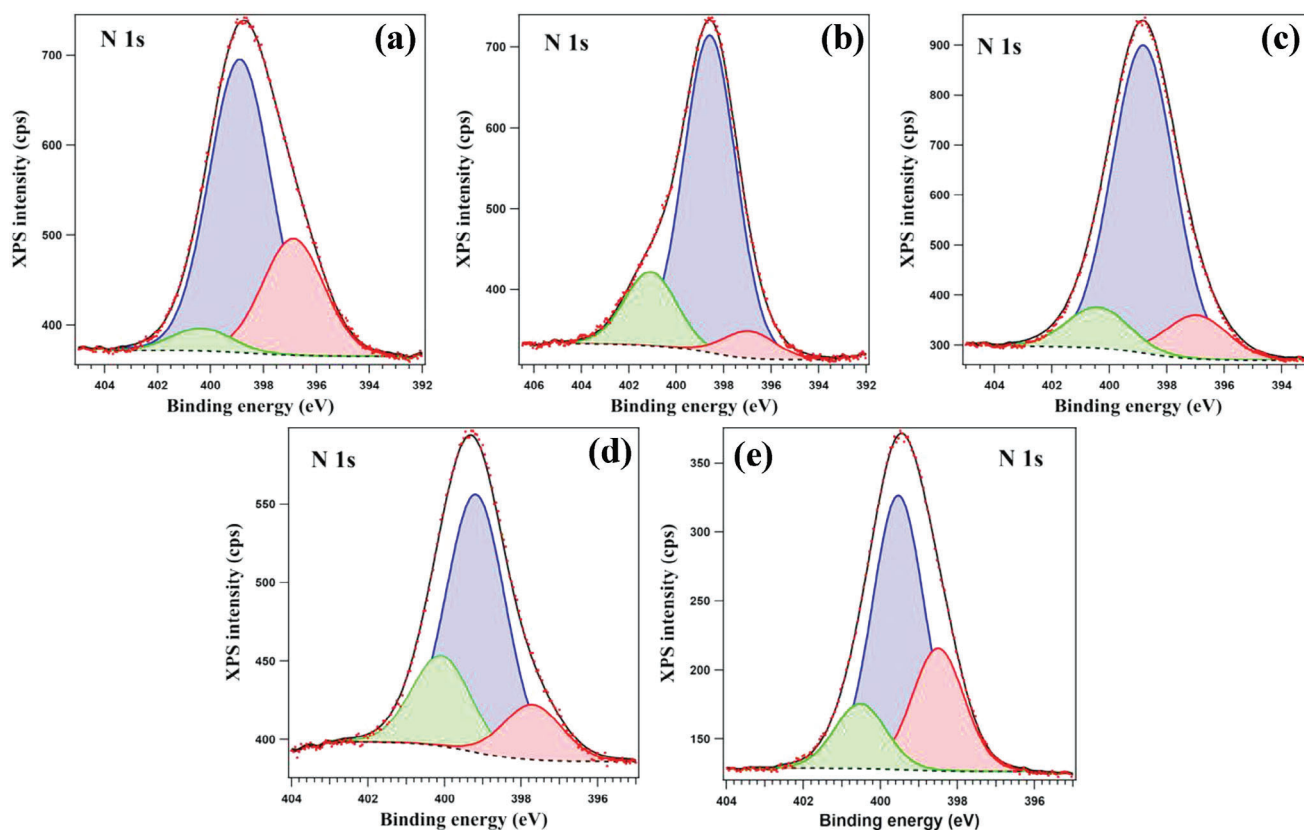


Figure 4. The XPS high-resolution of N1s spectrum of NCQDs: a) NCQDs-Urea, b) NCQDs-Alanine, c) NCQDs-Arginine, d) NCQDs-EDTA, e) NCQDs-Trizma.

carbon atoms in the carbon core. In contrast, the spectrum of NCQDs-Urea displays a sharp peak at the $\lambda_{\max} = 330$ nm, which is attributed to $n-\pi^*$ transitions of the nitrogen or oxygen containing group, and the absorption at 270 nm is related to the transition of sp^2 carbon. The variations in absorption bands and peak positions are indicative of differences in the electronic structure and chemical environment of the NCQDs.

The photoluminescent properties of all NCQDs were investigated. Diluted solutions of NCQDs were excited at various wavelengths, ranging from 280 to 400 nm with a 20 nm interval as (Figure 7). Interestingly, the synthesized NCQDs exhibit both independent and excitation dependent properties. The spectra of

NCQDs-Urea (Figure 7a) and NCQDs-Trizma (Figure 7e) show rarely observed excitation independent characteristic with emission peak position at 440 nm. The highest photoluminescent (PL) intensity is obtained at an excitation wavelength of 340 nm, and it diminishes significantly beyond $\lambda_{\text{ex}} = 360$ nm.

In contrast, the spectra of NCQDs-Alanine (Figure 7b) and NCQDs-Arginine (Figure 7c) demonstrate the typical excitation dependent emission. The PL emission of these NCQDs splits into two distinct regions, each exhibiting different responses to λ_{ex} . Excitation in the 280–340 nm range results in a dominant excitation-independent emission peak at 430 nm, corresponding to a single emissive transition. However, when the

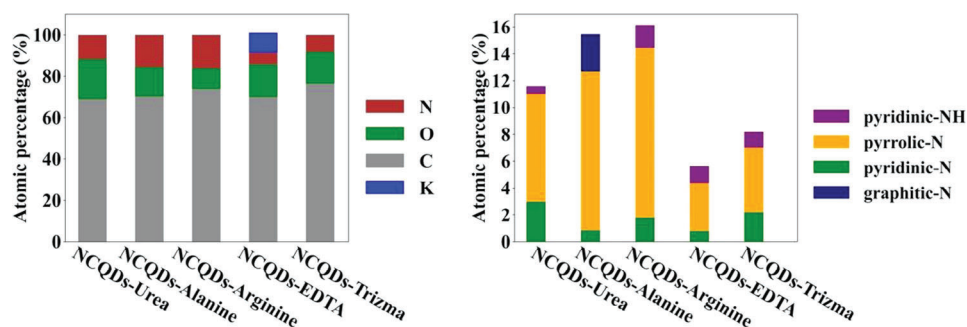


Figure 5. The XPS data of the synthesized NCQDs: a) the atomic composition and b) atomic percentage of nitrogen component.

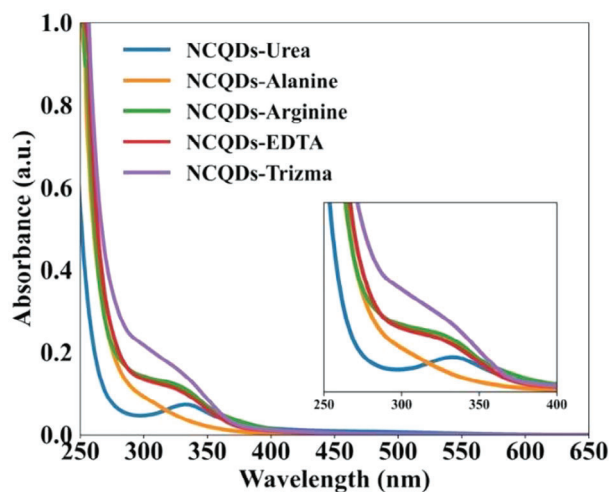


Figure 6. The UV-vis absorbance spectra of the synthesized NCQDs.

excitation wavelength is increased beyond 340 nm, the emission undergoes a redshift to longer wavelengths accompanied by significantly lower emission intensities. Similarly, NCQDs-EDTA (Figure 7d) exhibits excitation dependent emission, with the maximum emission wavelength at 460 nm ($\lambda_{\text{ex}} = 380$ nm).

Furthermore, the full width at half maximum (FWHM) of the emission spectra provides insights into the homogeneity of the emission source. The computed FWHM values (Table 2) for NCQDs-Trizma and NCQDs-Urea are 67 and 70 nm, respectively. Comparing these results to the commonly reported FWHM values of 100 nm for CQDs and to our previously reported work^[3] where ammonia was used as a dopant (FWHM of 78 nm), it becomes evident that NCQDs-Trizma and NCQDs-Urea exhibit excellent homogenous emission characteristics, correlating to their uniform particle size with narrow distribution observed from TEM data. In comparison, NCQDs-Alanine, NCQDs-Arginine and NCQDs-EDTA show a broad particle size distribution as reflected by a larger FWHM.

All as-synthesized NCQDs demonstrated comparable PL lifetimes, with NCQDs-Trizma and NCQDs-Arginine displaying PL lifetimes longer than 10 ns, which is rarely observed in carbon quantum dots materials.^[23] The computed k_r and k_{nr} rates indicate that NCQDs-Alanine and NCQDs-EDTA possess high non-radiative rates due to the surface defects acting as non-recombination centres, leading to lower PL lifetime and photoluminescence quantum yields (PLQY). These findings reveal the intricate interplay between the nitrogen dopants, particle size distribution, and surface defects in influencing the PLQY and PL lifetime of the NCQDs. By understanding these relationships, we can better tailor the synthesis process and optimize the optical properties of the NCQDs for targeted applications.

2.3. The Effect of Nitrogen Dopant in the Formation of NCQDs

Citric acid (CA), with its three carboxyl groups, is a multifunctional molecule that allows a variety of transformations through thermal dehydration, decarboxylation, and cyclization reactions. Under hydrothermal condition, CA can form five-

and six-membered anhydride structures that readily react with amines or alcohols to generate esters, polyesters, amides, and polyamides.^[24] Although CA itself isn't fluorescent, it can react with certain amines to produce an array of highly fluorescent compounds.^[25] However, the synthesis of CQDs from CA is highly sensitive to the synthesis conditions, such as decomposition temperature, residence time, and the type of nitrogen source used.^[26] The mechanism involved in the nucleation and growth of stable NCQDs from citric acid and nitrogen sources is complex and not yet fully understood.^[27] Different molecular precursors exhibit varied reactivities, leading to multiple concurrent chemical reactions, particularly under supercritical conditions. These complexities in the synthesis process contribute to the diversity in the optical properties and characteristics of NCQDs.

Indeed, the NCQDs synthesized using urea (NCQDs-Urea) and trizma base (NCQDs-Trizma) exhibited uniform particles with a narrow size distribution and excitation-independent fluorescence emission. In contrast, the use of β -alanine, L-arginine and EDTA resulted in NCQDs with a broader particle size distribution and excitation-dependent properties. The particle size distribution plays a critical role in understanding the formation of carbon quantum dots. A narrow distribution indicates controlled, homogeneous nucleation and growth, while a broader distribution reveals uneven particle formation kinetics.^[28]

During the CHFS process, supercritical water enables the hydrothermal synthesis of carbon quantum dots from citric acid. When an aqueous solution of citric acid is injected into water heated and pressurized above 374 °C and 22.0 MPa, the tricarboxylic acid rapidly ionizes and hydrolyses into fragments like citraconic and itaconic acids.^[29] This generates a multitude of molecular species that recombine into nuclei through esterification and decarboxylation pathways facilitated by the supercritical water. The carbon nanoparticle nuclei then undergo further growth through polymerization or carbonization reactions, leading to the formation of π -conjugated carbon core resembling subunits of graphene oxide composed of a heterogeneous sp^2 domain.^[30]

The observed variation in the size of the synthesized NCQDs confirms that the addition of nitrogen-containing precursors modifies the hydrothermal polymerization or carbonization pathway of citric acid. To understand the effects of nitrogen precursors, we compared the properties of the different nitrogen dopants (listed in Table 3). This comparison aims to reveal the key properties of the nitrogen sources that control nanoparticle sizes and size distribution.

The solubility of precursors significantly impacts nanoparticle formation in supercritical water. Precursors with higher solubility allow homogeneous dispersal and availability for nanoparticle nucleation.^[10,31] This is confirmed in the use of trizma base and urea which have excellent water solubility compared to the other nitrogen dopant precursors.

This high solubility allows uniform dispersal and availability of the nitrogen source during the carbonization process, leading to the formation of the sp^2 carbon domains more homogeneously and efficiently. Additionally, the alkaline conditions generated by trizma, and urea accelerate the dehydration of citric acid. This faster dehydration kinetics promotes a more rapid carbonization of citric acid.^[32] The dependence of nanoparticle size on the water solubility of nitrogen sources is also evident when using

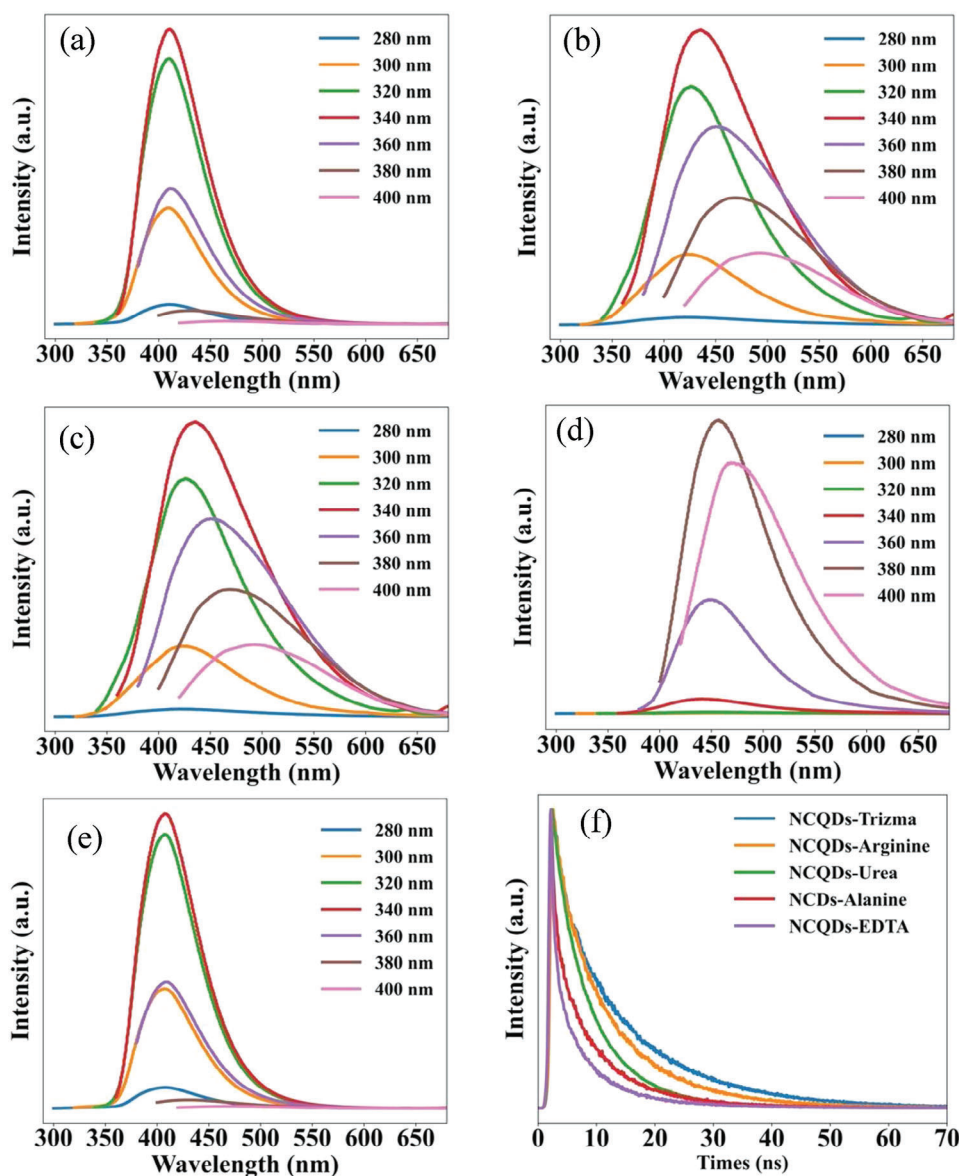


Figure 7. Excitation spectra of: a) NCQDs-Urea, b) NCQDs-Alanine, c) NCQDs-Arginine, d) NCQDs-EDTA, and e) NCQDs-Trizma, f) PL lifetime of the synthesized NCQDs.

β -alanine, L-arginine and EDTA. The limited water solubility of alanine, arginine and EDTA precursors disrupts the carbonization process leading to inconsistent nucleation and growth of the carbon core, and the formation of nanoparticles with a broad size distribution, as illustrated in Figure 2.

Furthermore, the decomposition process of the nitrogen precursors under supercritical water also plays a crucial role in causing variations in the structure and properties of the synthesized NCQDs. Citric acid and nitrogen dopants rapidly decompose via decarboxylation, dehydration, polymerization and carbonization reactions when subjected to CHFS.^[17] Urea and trizma base decompose at relatively lower temperatures compared to other nitrogen compounds used. Their decomposition temperatures are similar to that of citric acid (at 158 °C).^[33] The well-matched temperatures enable simultaneous carbonization of citric acid and re-

lease of nitrogen from urea and trizma for doping during carbon quantum dot formation. Additionally, neither urea nor trizma imparts a strong templating structure directing effect that alters particle formation from the carbonization of citric acid. The small size of the decomposed units from urea and trizma allows a homogeneous nucleation to produce uniform NCQDs.^[28]

In contrast, the smaller mean particle size of the prepared NCQDs-Alanine and NCQDs-Arginine suggest that β -alanine and L-arginine appear to limit nanoparticle growth due to steric hindrance of bulky groups in alanine and arginine interfering with crystallization and growth of the carbogenic π -conjugated domains.^[34] Additionally, the heterocyclic fragments from L-arginine can distort and limit nanoparticle growth.^[35] The freeze-dried NCQD synthesized using β -alanine and L-arginine displayed a sticky characteristic, indicating polymeric properties.

Table 2. The photoluminescence quantum yield (PLQY), PL lifetime of the synthesized NCQDs.

Sample	PLQY [%]	Average lifetime [ns]	Radiative k_r [s^{-1}]	Non-radiative k_{nr} [s^{-1}]	FWHM [nm]
NCQDs-Urea	14.0 ± 1.4	7.0 ± 0.7	1.5 × 10 ⁷	9.1 × 10 ⁷	70
NCQDs-Alanine	1.0 ± 0.1	8.0 ± 0.8	1.6 × 10 ⁶	1.5 × 10 ⁸	127
NCQDs-Arginine	5.0 ± 0.5	10.0 ± 1.0	4.2 × 10 ⁶	8.1 × 10 ⁷	81
NCQDs-EDTA	2.0 ± 0.2	6.5 ± 0.6	3.0 × 10 ⁶	2.0 × 10 ⁸	97
NCQDs-Trizma	40 ± 4.0	12.6 ± 1.2	3.5 × 10 ⁷	5.2 × 10 ⁷	67

This suggests β -alanine and L-arginine facilitate formation of short polymer chains that are retained due to incomplete carbonization during NCQD synthesis. The complex polymerization process likely leads to a highly crosslinked polydisperse network structure. This variation in the polymer structure influences the broad nanoparticle size distribution observed for these NCQDs. Recently, other groups have also reported about polymer-like CQDs using citric acid and amino acids.^[36,37] Similarly, EDTA possesses a large molecular weight and a high decomposition temperature leading to complex polymerization and incomplete carbonization processes. The intricate molecular structure, coupled with high thermal stability, causes uncontrolled nucleation and growth, yielding non-uniform nanoparticles. As shown in the Figure 2, the carbon dots synthesized using EDTA display a larger mean particle size and broad size distribution.

Based on characterization data collected about the morphology and optical properties of the synthesized NCQDs, we propose a mechanism for the conversion of citric acid and nitrogen precursors into fluorescent carbon nanomaterials via CHFS, as illustrated in Figure 8. The use of urea and trizma promote the crystallization and growth of the carbogenic π -conjugated domains resulting in highly crystallized NCQDs. However the decomposition of nitrogen precursors such as amino acids and EDTA, favors crosslinking and the formation of polymer-based structures indicating that polymerization is the primary reaction pathway. The abundance of functional groups allows for multiple reaction pathways, including esterification, decarboxylation, and condensation reactions, leading to the polymerization and carbonization of the nitrogen precursors. As a result, NCQDs with polymer-like characteristics are synthesized. As shown in Figure 8, the NCQDs-Urea and NCQDs-Trizma display blue emission under the UV light, and rarely observed excitation-independent emission. In contrast, the rest of the as-synthesized NCQDs showed a typical green excitation-dependent emission. Additionally, urea and trizma base yielded carbon dots with much higher PLQY compared to the other nitrogen precursors. In particular, trizma

Table 3. The chemical and physical properties of different nitrogen sources.

Chemical	Molecular weight [g mol ⁻¹]	Water solubility [g L ⁻¹]	Decomposition temperature [°C]	pH
Urea	60.06	624.00	160.00	9.5
β -Alanine	89.09	89.09	202.00	7.5
L-Arginine	174.20	182.00	220.00	8.0
EDTA	412.20	108.00	265.00	7.5
Trizma	121.14	678.00	143.00	10.6

resulted in carbon dots with a PLQY of \approx 40% which represents a significant improvement compared to our previous reports.^[3,4,11]

2.4. The Energy Band Structure of NCQDs

Ultraviolet photoemission spectroscopy (UPS) is a powerful technique widely employed to investigate the electronic structure and properties of various materials. The work function Φ , a fundamental parameter in materials science, plays a crucial role in determining the energy barrier for electron emission from a material's surface. It can be calculated using the formula:

$$\Phi = h\nu - E_k \quad (1)$$

where: Φ is the work function, h is the Planck constant, ν is the photon energy, and E_k is the kinetic energy of the emitted photoelectrons.^[38] By measuring the kinetic energy of emitted electrons, UPS enables the determination of the work function, providing valuable insights into the electron emission properties and surface characteristics of N-CQDs. The Fermi level, denoted as E_F , represents the energy level at which electrons have a 50% probability of being occupied at absolute zero temperature. It serves as a reference point for characterizing the energy distribution of electron states within a material. UPS enables the measurement of the Fermi level by observing the intensity variation of emitted photoelectrons as a function of incident photon energy. The position of the Fermi level provides crucial information about the electronic band structure and charge transport properties.^[39] In this study, we utilized UPS to investigate the electronic structure properties of nitrogen-doped carbon quantum dots. By measuring the work function, energy cut-off (E_{cutoff} , and Fermi level), we gain information into the surface electronic states, charge carrier dynamics, and the influence of nitrogen doping on the electronic properties of N-CQDs.

The UPS spectra, displayed in Figure 9a, exhibit variations in the measured energy E_{cutoff} of the synthesized nitrogen-doped carbon quantum dots (NCQDs), ranging from 15.37 to 15.32 eV. Consequently, the work function (WF) of the NCQDs falls within the range of 5.71 to 5.88 eV. The utilization of different nitrogen dopants resulted in distinct energy levels within the synthesized NCQDs, indicating varying degrees of surface modification in each sample. The optical bandgap of the synthesized nitrogen-doped carbon quantum dots was determined from UV-vis absorption spectra (Figure 6). The bandgap was calculated using the Tauc plot method,^[38] and the results are depicted in Figure 9c, showing the relationship between $(\alpha h\nu)^2$ and

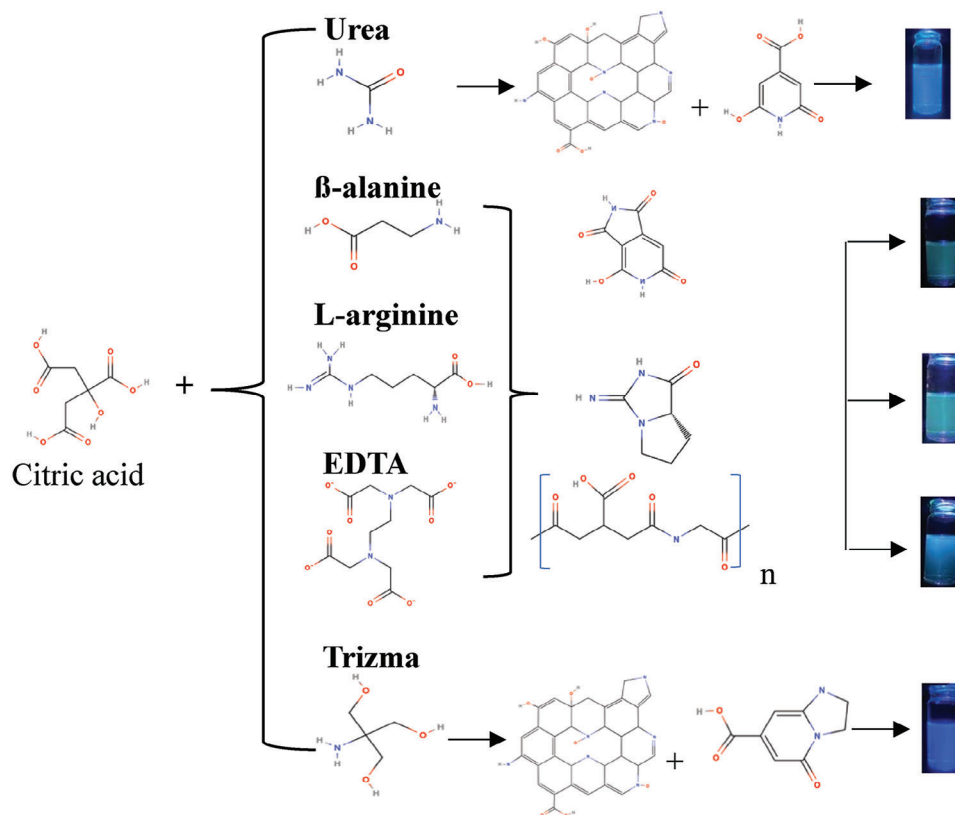


Figure 8. The NCQDs formation using different nitrogen precursors via CHFS method.

$h\nu$ (where α is the absorption coefficient and $h\nu$ is the photon energy). By extrapolating the straight sections of the curves in the short-wavelength region of the spectrum, the bandgap values of the NCQDs were estimated. The Tauc plots revealed that the bandgap of the NCQDs falls within the range of 4.66 to 4.94 eV. The energy band structure of the NCQDs is shown in Figure 10.

Hence, the bandgap of the synthesized nitrogen-doped carbon quantum dots (NCQDs) could be tuned by using different nitrogen dopants. The bandgap and energy level structure are influenced by both nanoparticle size and surface functional groups. The NCQDs prepared with urea (NCQDs-Urea) exhibited the largest bandgap (4.94 eV), attributed to the high content of pyrrolic-N, but a lower amount of protonated pyridinic-N as

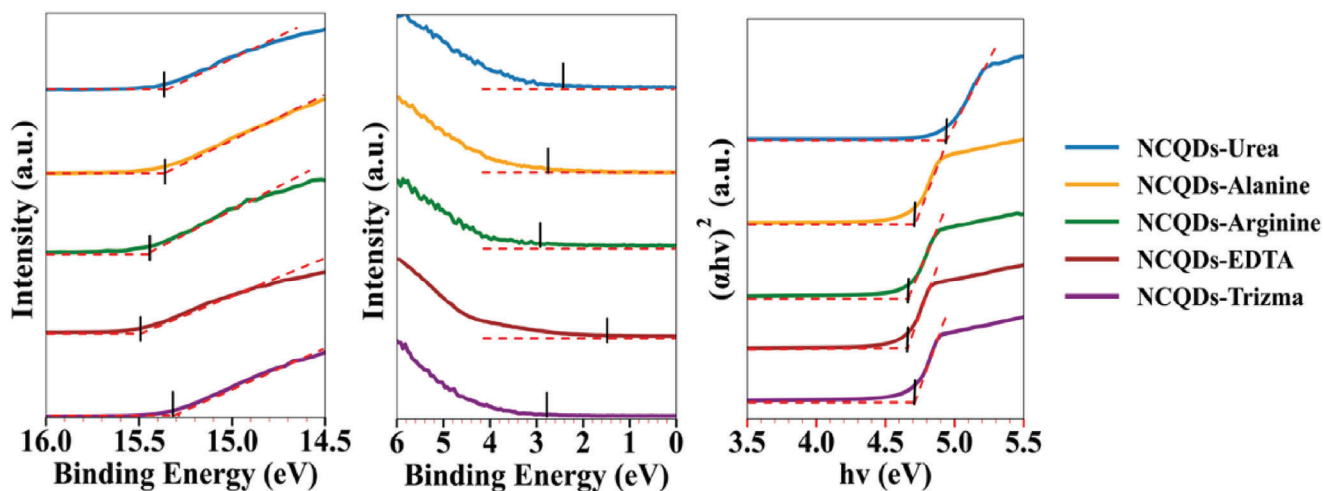


Figure 9. The UPS spectra of the NCQDs were used to determine the: (a) work function, (b) valence-band maximum, and (c) Tauc plots of NCQDs providing direct bandgap values.

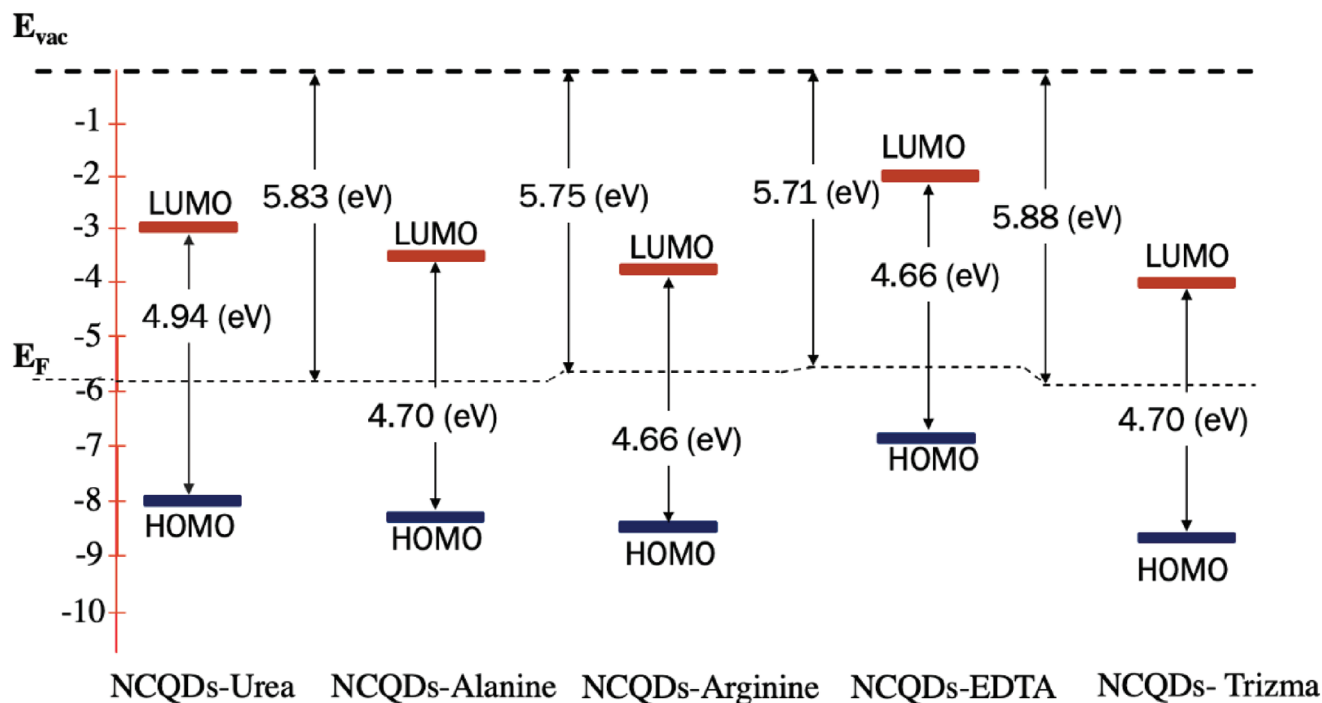


Figure 10. The energy band structure of the synthesized NCQDs.

evidenced by XPS. In contrast, the other synthesized NCQD samples showed similar, smaller bandgap values ≈ 4.70 eV. Additionally, NCQDs-Urea and NCQDs-Trizma displayed higher work functions, which correlates to their higher pyridinic-N content at the NCQD edges. To gain deeper insights into the effects of the surface functional groups in modifying the bandgap and work function, DFT and TD-DFT computational modelling was performed, as discussed in the next section.

2.5. Theoretical Insights

It has become customary to model carbon quantum dots as finite graphene fragments that include various defects and/or functional groups but are inherently single-layer structures.^[40] An obvious consideration is the size of these finite structures, which necessitates a balance between the physical reality and the computational costs. However, an often-overlooked aspect is the number of layers. While studying single-layer structures offers significant computational benefits, particularly in the context of high cost excited-state calculations, this approach might not offer the most accurate representation of a specific physical system. For example, as discussed, our synthesized NCQDs measure by AFM up to 4 nm in height (see Figure 1d). With a typical interlayer spacing of 0.35 nm, this would correspond to 12 layers in the structures (Table S1, Supporting Information). While this is clearly computationally challenging, a single layer might be an oversimplification and a compromise approach might be optimal. Herein, we show that a common approach of modelling single-layer structures is insufficient, but two layers suffice if one wants to reproduce the experimental data and not only study the trends.

In Figure 11a,b we show the calculated band gap and work function (WF) for the unmodified phenanthrene ($C_{14}H_{10}$), pyrene ($C_{16}H_{10}$), coronene ($C_{24}H_{12}$) and ovalene ($C_{32}H_{14}$) structures, ranging from 1 to 8 layers in AB stacking. Larger structures have smaller band gaps and WFs, which is to be expected. Single layer phenanthrene has a large bandgap and WF of 6.85 eV and 7.24 eV, which are lowered to 4.59 eV and 6.23 eV for ovalene, respectively. However, we are interested in the required number of additional layers for the values to level off. We see that adding a second and, in some cases, a third layer has the most pronounced effect, which then rapidly plateaus. This shows that from a band gap and WF perspective, it is rarely necessary to include more than three layers in the calculations. This is also justified by comparing these values with the measured band gaps of 4.66–4.94 eV and work functions of 5.71–5.88 eV for our NCQDs. They correlate well with the calculated values for ovalene (C_{32}), although the effects of functionalizing groups and defects must also be accounted for (see below). Finally, the predicted values for mixed structures (one layer of C_{32} and one layer of C_{14} , C_{16} or C_{24}) fall between their constituents. For example, for two-layer structures, we have: 2-layer C_{32} (4.34 and 5.96 eV), mixed $C_{32}+C_{24}$ (4.46 and 6.04 eV), 2-layers C_{24} (5.48 and 6.44 eV).

However, the fragment size and the number of layers have an even more pronounced effect on the absorption and emission spectra, as shown in Figure 11c,d. Smaller structures (C_{14} and C_{16}) have qualitatively different predicted spectra than the observed ones, while the difference between C_{24} and C_{32} is smaller. Most strikingly, the single-layer structures give completely different results than the two-layer structures, while adding a third layer negligibly affects the shape and peak positions in the spectra. Four-layer structures were prohibitively expensive to perform geometry optimization at the TD-DFT level.

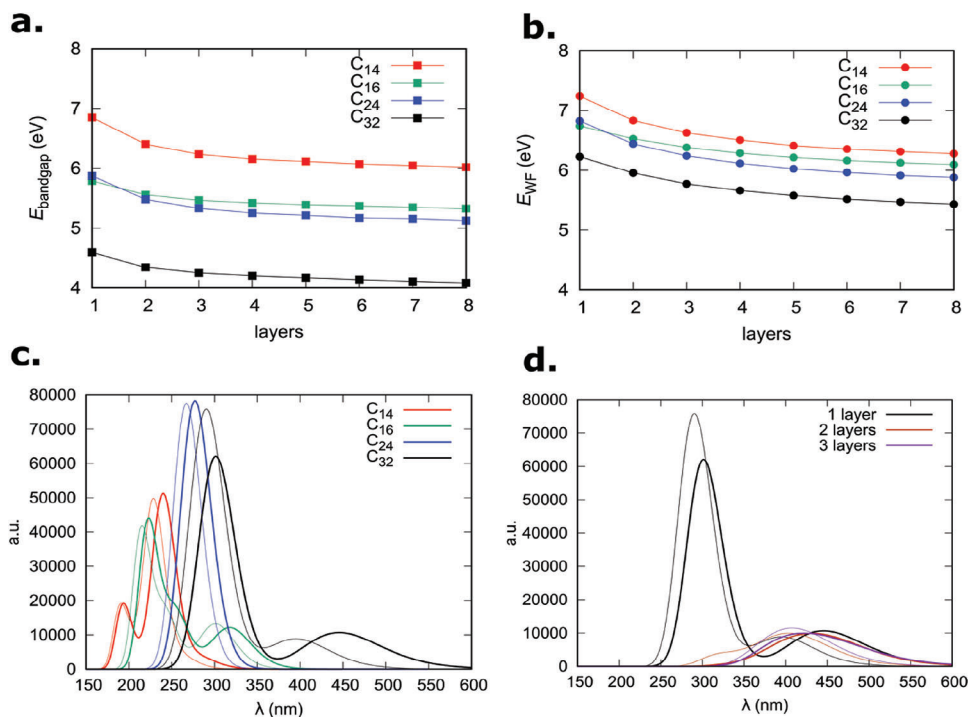


Figure 11. The calculated a) bandgaps and b) work functions for the unmodified phenanthrene ($C_{14}H_{10}$), pyrene ($C_{16}H_{10}$), coronene ($C_{24}H_{12}$) and ovalene ($C_{32}H_{14}$) structures of 1–8 layers, and their UV–vis absorption and emission spectra as function of c) the single-layer fragment size and d) the number of layers for ovalene. Thick and thin lines represent emission and absorption, respectively.

The implications of these findings vary depending on the aim of the theoretical predictions. When used to reproduce experimental results or guide synthesis, three-layer $C_{32}H_{14}$ structures offer the best compromise between accuracy and computational cost, although the latter is by no means small. However, single-layer structures are useful when we want to analyze the effects of different functionalizing groups and/or introducing defects. In this case, the use of smaller fragments allows for a finer control of the system and greater computational manageability. The results can then be either superimposed on the multi-layer analysis or re-run provided sufficient computational power is available. Therefore, we have used the single-layer C_{32} structure as a reference for our further analysis of the effects of modifications.

The introduction of different functionalizing groups (Figure 12), has a small effect on the band gap and work function, as shown in Table 4. The modifications can be divided into three types. Amide ($-\text{CONH}$), carboxyl ($-\text{COOH}$), amine ($-\text{NH}_2$), hydroxyl ($-\text{OH}$), and nitroso substituents ($-\text{NO}$) as well as the N-pyridine modification influence the band gap only insignificantly. Changes in the work function are more pronounced, as it can be increased (for amide, carboxyl, nitroso, N-pyridine) or decreased (amine, hydroxyl). The (de)protonated carboxyl and amine groups reduce the band gap only slightly, while the effects on the work function are not comparable in charged species.

Defects and modifications *within* the structure have a greater effect. The introduction of graphitic nitrogen decreases the band gap (and the WF) to 3.49 eV and 4.50 eV, respectively. A similar, yet smaller effect is achieved by carbon sp^2 vacancies. On the other hand, pyrrolic nitrogen and carbon sp^3 vacancies increase

both the bandgap and WF. In all instances, the effect is an order of magnitude greater compared to the functionalizing groups.

In Figure 13, we show emission spectra for differently modified single-layer ovalene. We see that the functionalizing groups, which weakly affect the bandgap and WF, do not significantly change the calculated spectra and only slightly shift the position of the peak. Typical changes of < 20 nm could be used to fine-tune the color of the emitted light but cannot bring about qualitative change (Figure 13a).

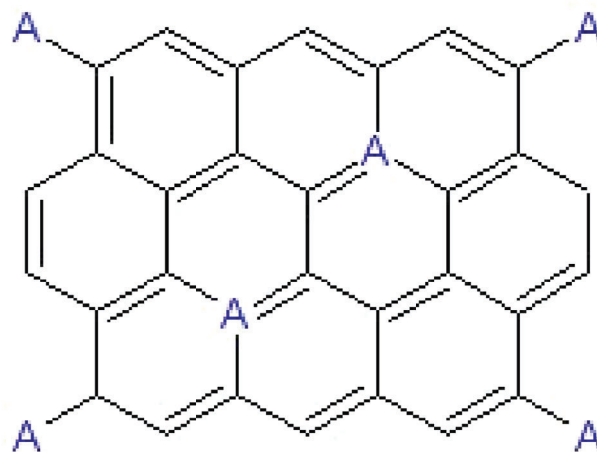


Figure 12. Single-layer structure of ovalene ($C_{32}H_{14}$), indicating (-A) where functionalizing groups or defects are introduced when studying their effects.

Table 4. The calculated bandgaps and work functions (WFs) for different modifications and/or defects in single layer ovalene, as shown in Figure 12. Note: For charges groups, only one group per ovalene is considered. For N-containing species, even number of groups are considered to ensure a singlet structure for comparability. All values in eV.

Functionalizing group / quantity	Bandgap [eV]				WF [eV]			
	1	2	3	4	1	2	3	4
none	4.59				6.23			
-CONH ₂	4.59	4.57	4.57	4.56	6.23	6.42	6.54	6.66
-COOH	4.58	4.52	4.52	4.52	6.32	6.49	6.61	6.73
-COO ⁻	4.40	–	–	–	3.72	–	–	–
-NH ₂	4.57	4.56	4.57	4.60	6.12	6.02	5.96	5.89
-NH ₃ ⁺	4.39	–	–	–	8.85	–	–	–
-OH	4.57	4.61	4.62	4.62	6.24	6.18	6.21	6.23
-NO	–	4.53	–	4.51	–	6.79	–	7.36
N-pyridine	–	4.60	–	4.65	–	6.59	–	6.99
N-graphitic	–	3.49	–	3.38	–	4.50	–	4.54
N-pyrrole	–	4.95	–	5.29	–	6.00	–	5.81
C-vacancy-sp ²	4.00	–	–	–	6.21	–	–	–
C-vacancy-sp ³	5.21	–	–	–	6.47	–	–	–

Increasing the number of the functionalizing groups has a negligible effect. On the other hand, introducing defects *within* the structure changes the spectra considerably. Graphitic nitrogen and unsaturated (sp²) C vacancies shift the peaks toward longer wavelengths, while pyrrolic nitrogen and saturated (sp³) C vacancies have the opposite effect.

An analysis of electron density and charge transfer provides additional information about the reason for the differences. In Figure 14, we show the charges on individual atoms in ovalene, as described by the NBO analysis.

The hydrogen atoms in unmodified ovalene are slightly positively charged (+0.21), while the adjacent carbon atoms are negatively charged (−0.17). Other carbon atoms in the molecule are almost neutral (−0.05). According to TD-DFT analysis, in the excited state, there is a flow of electron density from the carbon atoms (−0.08) towards the hydrogen atoms (+0.12). To visualise this electron density distribution more accurately, we plotted the differential electron density between the excited and ground state, which provides a clearer understanding of the flow of electrons upon excitations compared to analysing the HOMO and LUMO orbitals in the ground state. Our observations reveal that the presence of graphitic nitrogen atoms strongly influences the

electron density redistribution upon excitation, while functionalizing groups (only the amine group is plotted) do not have a significant impact. Therefore, it can be concluded that the excitation spectra are more influenced by the structural defects or substituents rather than functionalising groups.

3. Conclusion

The Continuous Hydrothermal Flow Synthesis process enabled the rapid and efficient production of nitrogen-doped carbon quantum dots. In this research, citric acid was employed as the carbon source, and various nitrogen dopants (urea, trizma base, beta-alanine, L-arginine and EDTA) were explored. The findings indicated that urea and trizma were particularly effective, contributing to the formation of NCQDs with superior quantum yields (up to 40%) and more homogeneous particle sizes when compared to those synthesized with amino acids of beta-alanine and L-arginine. These findings highlight the critical role of precursor reactivity, solubility, and molecular structure in the carbonization process. Urea and trizma facilitated the decarboxylation and dehydration of citric acid, which proved crucial for the formation of an optimal graphitic carbon core. On the other hand,

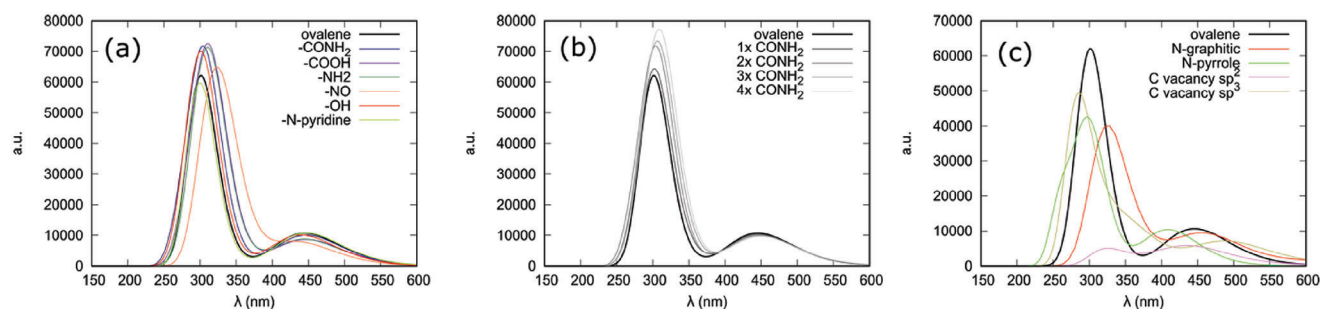


Figure 13. The emission spectra for single layer ovalene with a) different functionalizing groups, b) a different number of amide groups, c) different defects within the structure.

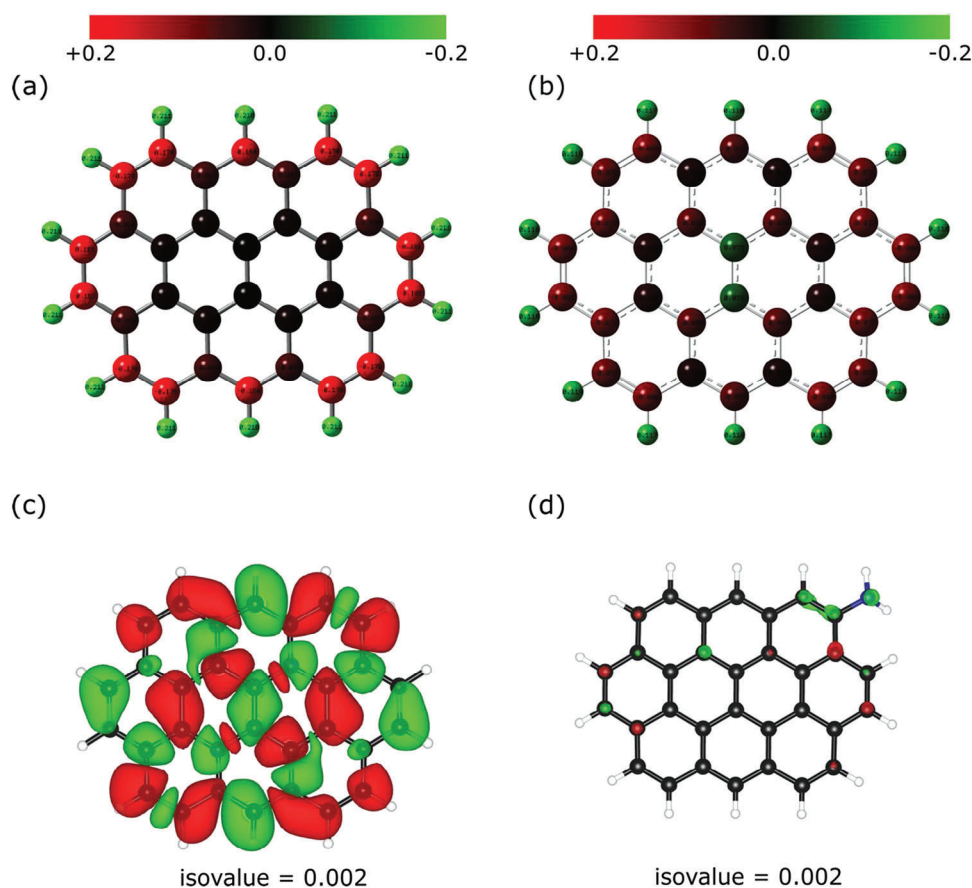


Figure 14. NBO calculated charges on non-modified ovalene in the a) ground state and b) excited state. Differential electron density between the excited state for c) 2N-graphitic substituted and d) NH₂-functionalised ovalene.

amino acids primarily led to polymerization pathways, resulting in a larger particle size distribution. Interestingly, we achieved excitation-independent emission for samples synthesized with urea and trizma, suggesting a uniform, single emissive state. A theoretical analysis further corroborated these findings, indicating that at least two layers of the graphitic structure need to be considered in any models to accurately reflect these experimental results. Functionalizing groups such as $-\text{NH}_2$, $-\text{COOH}$, $-\text{CONH}_2$, $-\text{OH}$, $-\text{NO}$, were found to have a relatively minor impact on the properties of NCQDs. This suggests that these groups can be utilized to fine-tune the emission properties, including color of the NCQDs. This effect was observed for a single-layer structure and is expected to remain consistent irrespective of the number of layers. Supporting this, electron analysis showed no significant activation or charge redistribution around the functionalizing groups upon excitation. In contrast, defects and substitutions, such as carbon vacancies or graphitic and pyrrolic nitrogen atoms, exerted a more pronounced influence on the properties of NCQDs.

In summary, this research provides valuable insights into the selection of appropriate nitrogen precursors to optimize PLQY, control particle sizes, and adjust optical properties of NCQDs. Additionally, it offers a deeper understanding of how precursor chemistry and nitrogen doping influence the formation of the carbon core, surface states, and photolumines-

cence. This knowledge can be instrumental for the future design and synthesis of tailored NCQDs for a wide array of applications.

4. Experimental Section

Materials: Citric acid (99.5%) and urea (99%) were purchased from Fisher Chemical (U.K.). Ethylenediaminetetraacetic acid dipotassium salt dihydrate, EDTA (99%), β -alanine (99%), L-arginine (99%) and trizma base (99%) were purchased from Sigma-Aldrich (U.K.). These were used as received without further modification. In addition, the deionized water (15 M Ω) from the ELGA Purelab system was used for all the experiments.

Synthetic Methodology: NCQDs were synthesized via the continuous hydrothermal flow synthesis (CHFS) process. In this study, citric acid (70.0 mg mL⁻¹) was used as carbon source, and a series of nitrogen precursors including urea (CH₄N₂O), EDTA (C₁₀H₁₆N₂O₈), β -alanine (C₃H₇NO₂), L-arginine (C₆H₁₄N₄O₂) and trizma base (C₄H₁₁NO₃), all with the same molarity of 1.0 M were utilized as nitrogen dopants.

The CHFS process^[9] consists of three pumps: the first pump (P1) delivered the deionized water, while the second (P2) and third pumps (P3) were used for carbon and nitrogen resources, respectively. Additionally, a back pressure regulator (BPR) was employed to maintain the system pressure at 24.8 MPa throughout the process. The deionized water was pumped through a heater set at 450 °C to reach a supercritical state, while the carbon and nitrogen precursors were mixed via a T junction at room temperature. The NCQDs were synthesized in a counter-current flow reactor where the supercritical water flows against the mixture of

carbon and nitrogen precursors. The reaction time (1.6 s) was controlled by the flowrate of the pumps. The following flowrates were used: P1 = 20.0 mL min⁻¹, P2 = 10.0 mL min⁻¹ and P3 = 10.0 mL min⁻¹. The samples were collected and cleaned with a molecular weight cut-off membrane of 30 kD, and denoted as NCQDs-Urea, NCQDs-Alanine, NCQDs-Arginine, NCQDs-EDTA, and NCQDs-Trizma.

Characterisation: The morphology of the synthesized NCQDs was investigated using high resolution transmission electron microscopy (HRTEM-JEOL ARM200F) and the images were analyzed using ImageJ software. The particles size analysis provided a useful insight about the effect of different precursors on particle size distribution. To gain a deeper understanding about the 3D shape of the synthesized NCQDs, the atomic force microscopy (AFM) was performed using an Asylum Research MFP-3D, operating in tapping mode, using Nanosensors PPP-NCL probes. AFM image processing included plane correction and scar removal using the built-in functions of the software. The IR Affinity-1S Fourier transform infrared (FT-IR) spectrometer was utilized to study the functional groups and chemical bonding detail of the synthesized materials. The FT-IR spectra were collected over a range of 400 – 4000 cm⁻¹. The Raman spectra of the as synthesized of NCQDs were collected using Renishaw in Via confocal Raman microscope. The NCQDs solutions were deposited into SERS-silver substrate, and the spectra were recorded using a 442 nm laser. The X-ray photoelectron spectroscopy (XPS) analysis was performed in an AXIS Ultra DLD (Kratos Surface Analysis) setup using Mg K α (1253.6 eV) radiation produced by a non-monochromatized X-ray source at operating power of 144 W (12 kV \times 12 mA). The base pressure in the analysis chamber was at least 1×10^{-9} mbar. The UV-Vis absorption spectra of the NCQDs solutions (0.1 optical density) were recorded using Shimadzu UV-1800 spectrophotometer. The spectra were measured in the range of 200–800 nm using a standard rate scan. The photoluminescence lifetime and the quantum yield were studied by using a FLS1000 photoluminescence spectrophotometer. The absolute quantum yield values of the NCQDs were measured by using an integrating sphere accessory and a standard method for aqueous samples was applied. The 375 nm laser was employed for PL lifetime measurement, while Xe lamp was used for PLQY measurements. Both PL lifetime and PLQY were measured using 0.1 optical density NCQDs solutions in 1.0 cm quartz cuvette. UPS measurements were performed using He I (21.2 eV) radiation source fitted in a Thermo NEXSA with a bias of -9 V. To further elucidate the effect of morphology and functional groups on the optical properties of the synthesized NCQDs, the theoretical calculations were performed using the density functional theory (DFT) level with a Minnesota-type functional (M06-2X) and the 6–311G (d,p) basis set. The M06-2X variant of the Minnesota family was chosen as it reproduces the thermochemistry of the main group elements best and the most broadly useful hybrid Minnesota functional.^[41] Ground-state properties were investigated with conventional DFT, while the excited-state properties were computed with the time-dependent DFT approach (TD-DFT). Accounting for ten excited states, first singlet excitations were considered for analysis. No solvent effect was included to keep the computational cost manageable (especially considering multi-layer structures were studied), which is warranted by the small effect of water on carbon quantum dots.^[42] To describe different NCQDs, finite fragments of the graphitic sheets were constructed. Effectively, the following polycyclic aromatic hydrocarbons were used: phenanthrene (C₁₄H₁₀), pyrene (C₁₆H₁₀), coronene (C₂₄H₁₂) and ovalene (C₃₂H₁₄), again finding a balance between the computational cost and experimentally determined NCQD size. We varied the functional groups and defects as well as the number of layers (1–8). Band gaps, absorption, and emission spectra, natural bond orbital (NBO) charges, structural deformation and electron density redistribution upon excitation were computed as implemented in Gaussian 16.

Supporting Information

Supporting Information is available from the Wiley Online Library or from the author.

Acknowledgements

K.N.G., S.K., and M.T.S. acknowledge the financial support provided by London South Bank University. The authors thank Dr Shaoliang Guan for his support with the UPS data collection which was performed at the EP-SRC National Facility for XPS (“HarwellXPS”), operated by Cardiff University and UCL, under Contract No. PR16195. M.H. appreciates financial support from the Slovenian Research Agency (ARRS) through project funding N1-0303 and J7-4638, core funding P2-0421, and infrastructure funding I0-0039. I.A.B., L.E.A., and A.N. would like to acknowledge the funding through the Core Program of the National Institute of Materials Physics, granted by the Romanian Ministry of Research, Innovation and Digitization through the Project PC3-PN23080303.

Conflict of Interest

The authors declare no conflict of interest.

Data Availability Statement

The data that support the findings of this study are available from the corresponding author upon reasonable request.

Keywords

continuous hydrothermal, DFT, N-doping, quantum dots

Received: November 17, 2023

Revised: February 4, 2024

Published online:

- [1] S. Yang, Y. Li, L. Chen, H. Wang, L. Shang, P. He, H. Dong, G. Wang, G. Ding, *Small* **2023**, *19*, 2205957.
- [2] S. Munusamy, T. R. Mandlimath, P. Swetha, A. G. Al-Sehemi, M. Pannipara, S. Koppala, P. Shanmugam, S. Boonyuen, R. Pothu, R. Boddula, *Environ. Res.* **2023**, *237*, 116046.
- [3] E. A. Stepanidenko, E. V. Ushakova, A. V. Fedorov, A. L. Rogach, *Nanomaterials* **2021**, *11*, 364.
- [4] V. M. Naik, S. V. Bhosale, G. B. Kolekar, *Anal. Methods* **2022**, *14*, 877.
- [5] X. Wang, Y. Feng, P. Dong, J. Huang, *Front. Chem.* **2019**, *7*, 671.
- [6] S. Wu, X. Wang, J. Bai, Y. Zhu, X. Yu, F. Qin, P. He, L. Ren, *Langmuir* **2022**, *38*, 11210.
- [7] Z. Yang, T. Xu, H. Li, M. She, J. Chen, Z. Wang, S. Zhang, J. Li, *Chem. Rev.* **2023**, *123*, 11047.
- [8] K. J. Mintz, Y. Zhou, R. M. Leblanc, *Nanoscale* **2019**, *11*, 4634.
- [9] I.-A. Baragau, N. P. Power, D. J. Morgan, T. Heil, R. A. Lobo, C. S. Roberts, M.-M. Titirici, S. Dunn, S. Kellici, *J. Mater. Chem. A* **2020**, *8*, 3270.
- [10] I.-A. Baragau, N. P. Power, D. J. Morgan, R. A. Lobo, M.-M. Titirici, V. Middelkoop, A. Diaz, S. Dunn, *ACS Sustainable Chem. Eng.* **2021**, *9*, 2559.
- [11] K. G. Nguyen, I.-A. Baragau, R. Gromicova, A. Nicolaev, S. A. J. Thomson, A. Rennie, N. P. Power, M. T. Sajjad, S. Kellici, *Sci. Rep.* **2022**, *12*, 13806.
- [12] U. Alli, S. J. Hettiarachchi, S. Kellici, *Chem. Eur. J.* **2020**, *26*, 6447.
- [13] J. D. Stachowska, A. Murphy, C. Mellor, D. Fernandes, E. N. Gibbons, M. J. Krysmann, A. Kellarakis, E. Burgaz, J. Moore, S. G. Yeates, *Sci. Rep.* **2021**, *11*, 10554.
- [14] Y. Song, S. Zhu, S. Zhang, Y. Fu, L. Wang, X. Zhao, B. Yang, *J. Mater. Chem. C* **2015**, *3*, 5976.

- [15] V. B. Kumar, S. K. Mirsky, N. T. Shaked, E. Gazit, *ACS Nano* **2024**, *18*, 2421.
- [16] M. C. Ortega-Liebana, M. M. Encabo-Berzosa, A. Casanova, M. D. Pereboom, J. O. Alda, J. L. Hueso, J. Santamaria, *Chem. Eur. J.* **2019**, *25*, 5539.
- [17] D. Qu, Z. Sun, *Mater. Chem. Front.* **2020**, *4*, 400.
- [18] S. D. Dsouza, M. Buerkle, P. Brunet, C. Maddi, D. B. Padmanaban, A. Morelli, A. F. Payam, P. Maguire, D. Mariotti, V. Svrcek, *Carbon* **2021**, *183*, 1.
- [19] L. Peplowski, R. Szczesny, L. Skowronski, A. Krupka, V. Smokal, B. Derkowska-Zielinska, *Vib. Spectrosc.* **2022**, *120*, 103377.
- [20] A. Pandey, A. Devkota, Z. Yadegari, K. Dumenyo, A. Taheri, *Nanomaterials* **2021**, *11*, 2012.
- [21] H. Lin, J. Huang, L. Ding, *J. Nanomater.* **2019**, *2019*, 1.
- [22] N. Papaioannou, A. Marinovic, N. Yoshizawa, A. E. Goode, M. Fay, A. Khlobystov, M.-M. Titirici, A. Sapelkin, *Sci. Rep.* **2018**, *8*, 6559.
- [23] L. Zhang, X. Yang, Z. Yin, L. Sun, *Luminescence* **2022**, *37*, 1612.
- [24] E. O. Miranda, V. H. R. Silva, M. A. Leão, E. C. M. Cabral-Albuquerque, S. Cunha, R. L. Fialho, *IOP Conf. Ser. Mater. Sci. Eng.* **2020**, *958*, 012008.
- [25] J. Schneider, C. J. Reckmeier, Y. Xiong, M. Von Seckendorff, A. S. Susha, P. Kasák, A. L. Rogach, *J. Phys. Chem. C* **2017**, *121*, 2014.
- [26] R. Ludmerczki, S. Mura, C. M. Carbonaro, I. M. Mandity, M. Carraro, N. Senes, S. Garroni, G. Granozzi, L. Calvillo, S. Marras, L. Malfatti, P. Innocenzi, *Chemistry* **2019**, *25*, 11963.
- [27] W. Kasprzyk, T. Świergosz, P. P. Romańczyk, J. Feldmann, J. K. Stolarczyk, *Nanoscale* **2022**, *14*, 14368.
- [28] N. T. K. Thanh, N. Maclean, S. Mahiddine, *Chem. Rev.* **2014**, *114*, 7610.
- [29] N. S. Kus, *Tetrahedron* **2012**, *68*, 949.
- [30] S. Kellici, J. Acord, N. P. Power, D. J. Morgan, T. Heil, P. Coppo, V. Middelkoop, I.-A. Baragau, K. E. Moore, C. L. Raston, *React. Chem. Eng.* **2018**, *3*, 949.
- [31] P. W. Dunne, C. L. Starkey, M. Gimeno-Fabra, E. H. Lester, *Nanoscale* **2014**, *6*, 2406.
- [32] X. Liu, H.-B. Li, L. Shi, X. Meng, Y. Wang, X. Chen, H. Xu, W. Zhang, X. Fang, T. Ding, *J. Mater. Chem. C* **2017**, *5*, 10302.
- [33] P. Wicinska, *J. Therm. Anal. Calorim.* **2016**, *123*, 1419.
- [34] T. Morris, T. Zubkov, *Colloids Surf. Physicochem. Eng. Asp.* **2014**, *443*, 439.
- [35] I. M. Weiss, C. Muth, R. Drumm, H. O. K. Kirchner, *BMC Biophys.* **2018**, *11*, 2.
- [36] A. Kolanowska, G. Dzido, M. Krzywiecki, M. M. Tomczyk, D. Łukowiec, S. Ruczka, S. Boncel, *ACS Omega* **2022**, *7*, 41165.
- [37] C. Xia, S. Zhu, T. Feng, M. Yang, B. Yang, *Adv. Sci.* **2019**, *6*, 1901316.
- [38] N. Bhalla, S. Taneja, P. Thakur, P. K. Sharma, D. Mariotti, C. Maddi, O. Ivanova, D. Petrov, A. Sukhachev, I. S. Edelman, A. Thakur, *Nano Lett.* **2021**, *21*, 9780.
- [39] Y. Yan, J. Chen, N. Li, J. Tian, K. Li, J. Jiang, J. Liu, Q. Tian, P. Chen, *ACS Nano* **2018**, *12*, 3523.
- [40] J. Feng, Q. Guo, N. Song, H. Liu, H. Dong, Y. Chen, L. Yu, L. Dong, *Diam Relat Mater* **2021**, *113*, 108264.
- [41] N. Mardirossian, M. Head-Gordon, *J. Chem. Theory Comput.* **2016**, *12*, 4303.
- [42] S. H. Jin, D. H. Kim, G. H. Jun, S. H. Hong, S. Jeon, *ACS Nano* **2013**, *7*, 1239.